

## TUNABLE COLLISIONS: HAMMER-STRING SIMULATION WITH TIME-VARIANT PARAMETERS

Maarten van Walstijn and Abhiram Bhanuprakash

SARC  
Queen's University Belfast  
Belfast, UK  
{m.vanwalstijn|abhanuprakash01}@qub.ac.uk

Vasileios Chatziioannou

Department of Music Acoustics (IWK)  
University of Music and Performing Arts  
Vienna, Austria  
chatziioannou@mdw.ac.at

### ABSTRACT

In physical modelling synthesis, articulation and tuning are effected via time-variation in one or more parameters. Adopting hammered strings as a test case, this paper develops extended forms of such control, proposing a numerical formulation that affords on-line adjustment of each of its scaled-form parameters, including those featuring in the one-sided power law for modelling hammer-string collisions. Starting from a modally-expanded representation of the string, an explicit scheme is constructed based on quadratising the contact energy. Compared to the case of time-invariant contact parameters, updating the scheme's state variables relies on the evaluation of two additional analytic partial derivatives of the auxiliary variable. A numerical energy balance is derived and the numerical contact force is shown to be strictly non-adhesive. Example results with time-variant tension and time-variant contact stiffness are detailed, and real-time viability is demonstrated.

### 1. INTRODUCTION

The manipulation of variables is intrinsic to musical instrument performance. For example, to produce a specific sound with a violin the musician controls the speed, normal force, and angle of the bow as well as the position of fingers that press the string to the fingerboard. In hammered string instruments, which is the target of the current study, such articulation is normally restricted to the acceleration of keys that drive the hammer motion and the adjustment of tension during the tuning process, although in certain instrument families, such as dulcimers, the striking position on the string can also be varied.

In musical instrument modelling, articulation and tuning are accomplished through variation over time of the relevant physical parameters. This is exploited in physics-based synthesis for the exploration of the sound of acoustic instruments (of both existing and modular design) across their parameter spaces [1]. Recently, specific attention has been given to on-line tuning of parameters that are normally considered to remain constant [2, 3]. To contribute towards facilitating such extended synthesis control, this paper sets out to numerically model the interaction between a hammer and a stiff string under time-variance of a non-redundant set of model parameters. For the resulting algorithm to be of practical use, it should be computationally efficient, numerically stable, and free of audible artefacts. In addition, the response to driving forces

and parameter manipulations should ideally be similar to what can be expected in that regard from the underlying physical laws, and parameter time-variance should not necessarily lead to large amplitude swings in the chosen output signal.

Solutions to various similar and related problems can be found across the literature. Most notably, simulation of string vibrations under time-varying tension (or an equivalent string length adjustment) has been reported using digital waveguides [4], mass-spring-damper systems [5], finite-difference methods [3], and modal synthesis [6]. The challenge increases when nonlinearities are introduced, perhaps most tellingly so when one-sided forces are involved. For example, models in which a finger or other object can be dynamically brought in contact with a string while also its position along the string axis can be varied over time (e.g. [7, 8]) typically rely on an iterative solver to update the state variables, which severely reduces the scope for parallelisation and real-time implementation [9]. Similarly, in [2] all 29 parameters of a modal-form string-bridge-plate model with nonlinear spring connections were made tunable, but the use of an iterative solver meant that for real-time audio rendering the parameter space and the rate of change in parameters had to be empirically constrained to avoid instability issues and artefacts. In [10] this issue was side-stepped by casting the update equations in analytic form, but so far this has been made to work only for a small subset of cases in which a unity contact power law exponent applies.

Originating separately in Port-Hamiltonian form [11], the recent emergence of energy quadratisation approaches, including the Invariant Energy Quadratisation (IEQ) method [12] and the Scalar Auxiliary Variable (SAV) method [13], has paved the way for numerical simulation of nonlinear musical instruments vibrations without the use of iterative solvers [14, 15], with specific scheme variants introduced for modelling collisions [16, 17]. The current paper extends energy quadratisation to modelling lumped conservative nonlinearities under parameter time-variance, taking hammer-string interaction as a case study. For completeness, additional innovations that improve the handling of tension time-variance in modal-form algorithms are introduced.

The paper is structured as follows. The hammer-string system equations are outlined in Section 2, including a scaled form that is modally expanded. The discretisation of the resulting equations is presented in Section 3, with the update equations provided and also featuring analyses of the key properties of the resulting algorithm. The proposed formulation is then explored, exemplified, and tested in Section 4 via a number of numerical experiments, followed by concluding remarks in Section 5. Sound examples are available on the accompanying github page<sup>1</sup>.

Copyright: © 2023 Maarten van Walstijn et al. This is an open-access article distributed under the terms of the Creative Commons Attribution 4.0 International License, which permits unrestricted use, distribution, adaptation, and reproduction in any medium, provided the original author and source are credited.

<sup>1</sup><https://github.com/mvanwalstijn/Tunable-Collisions>

## 2. HAMMER-STRING MODEL

In the following,  $\partial_t y$  and  $\partial_x y$  denote the partial derivatives with respect to time  $t$  and string axis position  $x$ , respectively, and the total time derivative is written as  $d_t y$ . Considering a string of length  $L$ , mass density  $\rho$ , cross section  $A$ , Young's modulus  $E$ , moment of inertia  $I$  interacting with a hammer of mass  $m_h$  striking from above, the equations governing the transversal string displacement  $u = u(x, t)$  and hammer position  $u_h = u_h(t)$  can be written as [18]:

$$\rho A \partial_t^2 u = T \partial_x^2 u - EI \partial_x^4 u + \theta(x) F_c, \quad (1)$$

$$d_t \{m_h d_t u_h\} = F_e - F_c. \quad (2)$$

The driving of the hammer is represented here with the excitation force  $F_e = F_e(t)$ , the specific form of which depends on the type of instrument. For example, a simplified form of modelling  $N_p$  successive piano hammer strikes at time instants  $t = \tau_i$  is:

$$F_e(t) = \sum_{l=1}^{N_p} \underbrace{m_h V_{e,l}}_{p_{e,l}} \delta(t - \tau_l) + F_{\text{stop},l}(t), \quad (3)$$

where  $V_{e,l} < 0$  is an externally supplied hammer velocity parameter. In the absence of gravity, we emulate the hammer coming to rest at  $u_h = u_{\text{max}}$  after bouncing back from the string, which is represented in (3) by the forces  $F_{\text{stop},l}(t) < 0$ ; in practice, one may achieve this by simply capping the hammer displacement at  $u_h = u_{\text{max}}$ . Modelling the driving of the hammer in dulcimers or clavichords would require different formulations of  $F_e(t)$ .

The contact force in (1,2) is assumed to be non-hysteretic under parameter constancy, and is defined with a power-law:

$$F_c = -\kappa [y]_+^\alpha \leq 0, \quad (4)$$

where  $[y(t)]_+ = \max(0, u_s(t) - u_h(t))$  is the effective inter-object compression. For simplicity, the contact force is applied at a single point, using  $\theta(x) = \delta(x - x_h)$ . Correspondingly, the displacement of the string as 'seen' by the hammer is  $u_s(t) = u(x_h, t)$ . Simply supported boundary conditions are assumed:

$$u(0, t) = \partial_x^2 u(0, t) = 0, \quad u(L, t) = \partial_x^2 u(L, t) = 0, \quad (5)$$

and initial conditions are set as

$$u_h(0) = u_{\text{max}}, \quad d_t u_h(0) = 0, \quad u(x, 0) = 0, \quad \partial_t u(0, x) = 0. \quad (6)$$

As in previous studies (e.g. [10]), the force at the end of the string is chosen as an appropriate output variable:

$$F_s(t) = -T \partial_x u(L, t) + EI \partial_x^3 u(L, t). \quad (7)$$

### 2.1. Scaled Form

The parameters  $\rho$ ,  $A$ , and  $L$  are considered to remain constant over time. To obtain a form of the system equations with fewer parameters, the following non-dimensional variables are introduced:

$$\bar{x} = \frac{x}{L}, \quad \bar{u} = \frac{u}{L}, \quad \bar{u}_h = \frac{u_h}{L}. \quad (8)$$

Then, after substitution, the system can be written as

$$\partial_t^2 \bar{u} = \bar{T} [\partial_{\bar{x}}^2 \bar{u} - \pi^{-2} \mathcal{B} \partial_{\bar{x}}^4 \bar{u}] + \bar{\theta}(\bar{x}) \bar{F}_c, \quad (9)$$

$$d_t \{\bar{m}_h d_t \bar{u}_h\} = \bar{F}_e - \bar{F}_c, \quad (10)$$

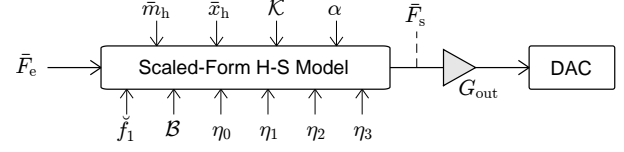


Figure 1: Schematic diagram of the scaled-form hammer-string model.

where

$$\bar{F}_c = \bar{\kappa} [\bar{u}_s - \bar{u}_h]_+^\alpha, \quad \bar{F}_e = \sum_l^{N_p} \frac{\bar{p}_{e,l}}{\rho A L^2} \delta(t - \tau_l), \quad (11)$$

$$\bar{m}_h = \frac{m_h}{\rho A L}, \quad \bar{T} = \frac{T}{\rho A L^2}, \quad \mathcal{B} = \frac{EI \pi^2}{T L^2}, \quad (12)$$

$$\bar{\kappa} = \frac{\kappa L^{\alpha-2}}{\rho A}, \quad \bar{x}_h = \frac{x_h}{L}, \quad \bar{\theta}(\bar{x}) = \delta(\bar{x} - \bar{x}_h). \quad (13)$$

The new parameter  $\mathcal{B}$  is the inharmonicity factor [19],  $\bar{m}_h$  is the hammer/string mass ratio, and  $\bar{u}_s(t) = \bar{u}(\bar{x}_h, t)$ . Analogously, we may define

$$\bar{F}_s(t) = \frac{F_s}{\rho A L^2} = \bar{T} [\pi^{-2} \mathcal{B} \partial_{\bar{x}}^3 - \partial_{\bar{x}}] \bar{u}(1, t). \quad (14)$$

### 2.2. Energy Quadratisation

The scaled-form contact force in (11) can be expressed as:

$$\bar{F}_c = -\partial_{\bar{y}} \bar{\Phi}, \quad \bar{\Phi}(\bar{y}) = \frac{\bar{\kappa}}{\alpha + 1} [\bar{y}]_+^{\alpha+1}, \quad (15)$$

where the actual contact potential  $\Phi$  (in Joules) relates to its scaled-form counterpart as  $\Phi = \rho A L^3 \bar{\Phi}$ . Taking a split-potential energy quadratisation approach [15], the scaled-form contact potential is written in quadratic form with  $\bar{\Phi} = \frac{1}{2} \psi^2$ . Making use of the chain rule, this allows writing the contact force as

$$\bar{F}_c = -\psi \overbrace{\partial_{\bar{y}} \psi}^{g_{\bar{y}}} = -\psi \frac{d_t \psi - d_t \bar{\kappa} \overbrace{\partial_{\bar{\kappa}} \psi}^{g_{\bar{\kappa}}} - d_t \alpha \overbrace{\partial_{\alpha} \psi}^{g_{\alpha}}}{d_t \bar{y}}. \quad (16)$$

Defining the auxiliary variable  $\psi$  as the positive square root of  $2\bar{\Phi}$ , the gradient variables  $g_{\bar{y}}$ ,  $g_{\alpha}$ , and  $g_{\bar{\kappa}}$  can be expressed directly as functions of  $\bar{y}$ ,  $\alpha$ , and  $\bar{\kappa}$  as follows:

$$g_{\bar{y}} = \sqrt{\frac{1}{2} \bar{\kappa} (\alpha + 1)} [\bar{y}]_+^{\alpha-1}, \quad g_{\bar{\kappa}} = \sqrt{\frac{[\bar{y}]_+^{\alpha+1}}{2 \bar{\kappa} (\alpha + 1)}} \quad (17)$$

$$g_{\alpha} = \sqrt{\frac{\frac{1}{2} \bar{\kappa} [\bar{y}]_+^{\alpha+1}}{\alpha + 1}} \left[ \log([\bar{y}]_+ + \varepsilon) - \frac{1}{\alpha + 1} \right], \quad (18)$$

where a positive constant of the size of the machine epsilon has been included within the log term in (18) for handling the case where  $[\bar{y}]_+$  approaches zero. Following similar principles as applied in IEQ and SAV methods, the numerical scheme will be constructed in explicit form by directly discretising the equations contained within (16) and making use of the analytic expressions in (17,18) to evaluate the gradient variables. A novel aspect is the emergence of the additional gradient terms  $g_{\alpha}$  and  $g_{\bar{\kappa}}$  due to time variance in the power law parameters. It is worth noting that if  $\psi$  is defined as  $-\sqrt{2\bar{\Phi}}$ , for consistency the terms  $g_{\bar{y}}$ ,  $g_{\bar{\kappa}}$  and  $g_{\alpha}$  would also have to have a minus sign in front of the square root symbol.

### 2.3. Parameter Control

Figure 1 shows the inputs and outputs of the scaled-form model. The output gain  $G_{\text{out}}$  is needed to scale  $\bar{F}_s$  to the  $[-1, 1]$  input range of the digital-to-analog converter. Each of the ten control parameters in Figure 1 is considered to be adjustable on the fly, and as such is treated as time-dependent. Four of those parameters ( $\mathcal{B}$ ,  $\bar{m}_h$ ,  $\bar{x}_h$ , and  $\alpha$ ) readily appear in the scaled-form model equations (9-13). The parameters  $\eta_{0,1,2,3}$  are damping coefficients that will be introduced in Section 2.4. This subsection explains how the remaining two parameters ( $\check{f}_1$ ,  $\mathcal{K}$ ) are related to the scaled-form model parameters. The tension parameter ( $\bar{T}$ ) can be calculated directly from the string's fundamental frequency  $\check{f}_1$  (in Hz) in the absence of stiffness as  $\bar{T} = 4\check{f}_1^2$ . To enable independent control of the effective stiffness (through  $\mathcal{K}$ ) and the 'contact nonlinearity' (through  $\alpha$ ),  $\bar{\kappa}$  has been re-parameterised as follows:

$$\bar{\kappa} = (\alpha + 1)\mathcal{K} \left( \frac{\mathcal{K}}{\bar{\Phi}_r} \right)^\alpha. \quad (19)$$

where  $\bar{\Phi}_r$  denotes a (constant-over-time) scaled-form reference potential that represents the amount of contact energy that can approximately be expected<sup>2</sup>. This is exemplified in Figure 2. Example values for the control parameters, which were transcribed from [20], are listed in Table 1. Where needed, the string constants  $\rho A$  and  $L$  are used for un-scaling displacements, forces, or energies, but they do not otherwise feature within the scaled-form model that forms the basis for numerical simulation.

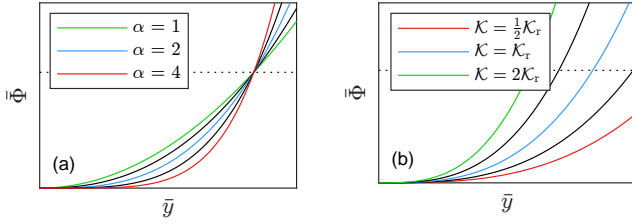


Figure 2: Contact potential curves for (a): a range of  $\alpha$  values with  $\mathcal{K} = \mathcal{K}_r$  and (b): a range of  $\mathcal{K}$  values and  $\alpha = 2$ . In both subfigures, the horizontal dashed line indicates the scaled-form reference potential ( $\bar{\Phi}_r$ ).

### 2.4. Modal Expansion

For the boundary conditions in (5), we may expand the string displacement as

$$\bar{u}(\bar{x}, t) = \sum_{i=1}^M \underbrace{\sqrt{2} \sin(i\pi\bar{x}(t))}_{v_i(\bar{x}(t))} \tilde{u}_i(t) = [\mathbf{v}(\bar{x})]^T \mathbf{u}, \quad (20)$$

where  $v_i(\bar{x}(t))$  and  $\tilde{u}_i(t)$  are the modal shape function and the modal displacement for the  $i$ th mode, and  $\mathbf{v}(\bar{x})$  and  $\mathbf{u}$  are the respective column vector representations (with time dependence dropped in the notation). Substituting (20) into (9), multiplying with the basis functions, and spatially integrating from  $\bar{x} = 0$  to

<sup>2</sup>The  $\mathcal{K}$  values in Table 1 have been transcribed using  $\bar{\Phi}_r \approx 0.75/L^2$ , which is a representative value of the average piano key, derived from setting the unscaled version  $\Phi_r$  equal to the kinetic energy of a hammer with  $\bar{m}_h = 0.75$  and  $d_t u_h = -1.41$  m/s.

Table 1: Scaled-form model parameter values (transcribed from [20]).

	piano C2	piano C4	piano C7
$\check{f}_1$ [Hz]	65.4	262	2093
$\mathcal{B}$	$7.4 \times 10^{-5}$	$3.77 \times 10^{-4}$	$8.6 \times 10^{-3}$
$\eta_0$ [ $s^{-1}$ ]	0.5	0.5	0.5
$\eta_1$ [ $s^{-1}$ ]	0.01	0.01	0.1
$\eta_2$ [ $s^{-1}$ ]	0.0	0.0	0.0
$\eta_3$ [ $s^{-1}$ ]	$10^{-6}$	$10^{-6}$	$10^{-4}$
$\bar{m}_h$	0.14	0.75	4.71
$\mathcal{K}$ [ $s^{-2}$ ]	335	2560	$4.3 \times 10^4$
$\alpha$	2.3	2.5	3.0
$\bar{x}_h$	0.12	0.12	0.0625
$\rho A$ [ $kg\ m^{-1}$ ]	$18.4 \times 10^{-3}$	$6.3 \times 10^{-3}$	$5.2 \times 10^{-3}$
$L$ [m]	1.90	0.62	0.09

$\bar{x} = 1$  then leads to a set of coupled ordinary differential equations which may be expressed in vector form as

$$d_t^2 \mathbf{u} + \mathbf{R} d_t \mathbf{u} + \mathbf{K} \mathbf{u} = \mathbf{h} \bar{F}_c, \quad (21)$$

where  $\mathbf{h} = \mathbf{v}(\bar{x}_h)$  and  $\mathbf{K}$  is an  $M \times M$  diagonal matrix with the non-zero elements

$$K_{i,i} = i^2 \pi^2 \bar{T} (1 + \mathcal{B} i^2). \quad (22)$$

Initially, since there is no string damping in (9), the  $M \times M$  damping matrix  $\mathbf{R}$  contains only zeros. String damping can be introduced in polynomial form by setting the diagonal elements of  $\mathbf{R}$  to:

$$R_{i,i} = 2 (\eta_0 + \eta_1 i \pi + \eta_2 i^2 \pi^2 + \eta_3 i^3 \pi^3). \quad (23)$$

Of particular relevance is the case where  $\eta_2 = 0$ , which can be shown (see [2]) to align well with the experimentally validated damping formulation by Woodhouse [21]. The  $i$ th mode frequency for free vibration (i.e.  $\bar{F}_i = 0$ ) then is

$$\omega_i = \sqrt{K_{i,i} - \frac{1}{4} R_{i,i}^2}, \quad (24)$$

which takes on an imaginary value in case of overdamping. In modal form, the string displacement at the contact point can be written as  $u_s = \mathbf{h}^T \mathbf{u}$ , and the string force in (14) becomes

$$\bar{F}_s(t) = - \sum_{i=1}^M \underbrace{i\pi\bar{T}(t) [1 + \mathcal{B}(t)i^2]}_{w_i(t)} (-1)^i \tilde{u}_i(t) = -\mathbf{w}^T \mathbf{u}. \quad (25)$$

The direct dependence of  $w_i$  on  $\bar{T}$  can lead to large swings in the output amplitude when time-varying the string tension. The need for output gain adjustments can be significantly reduced by replacing  $w_i(t)$  with the adjusted output weights  $\hat{w}_i(t) = \sqrt{\frac{\bar{T}(0)}{\bar{T}(t)}} w_i(t)$ .

### 2.5. Energy Balance and Conserved Quantities

An energy balance equation can be obtained by pre-multiplying (21) with  $(d_t \mathbf{u})^T$ , multiplying (10) with  $d_t \bar{u}_h$ , and adding the resulting equations, yielding

$$d_t \bar{H} = \frac{1}{2} \mathbf{u}^T (d_t \mathbf{K}) \mathbf{u} - (d_t \mathbf{u})^T \mathbf{R} d_t \mathbf{u} - (d_t \mathbf{h})^T \mathbf{u} \bar{F}_c + d_t \bar{u}_h \bar{F}_c - (d_t \bar{u}_h)^2 d_t \bar{m}_h + \psi (g_{\bar{\kappa}} d_t \bar{\kappa} + g_{\alpha} d_t \alpha), \quad (26)$$

in which the scaled-form Hamiltonian  $\bar{H}$  takes the form :

$$\bar{H} = \frac{(d_t \mathbf{u})^T d_t \mathbf{u}}{2} + \frac{\mathbf{u}^T \mathbf{K} \mathbf{u}}{2} + \frac{\bar{m}_h (d_t \bar{u}_h)^2}{2} + \frac{\psi^2}{2} \geq 0. \quad (27)$$

From (10) and (26), it is immediately clear that the scaled-form hammer momentum  $\bar{p}_h = \bar{m}_h d_t \bar{u}_h$  and system Hamiltonian  $\bar{H}$  are conserved under specific conditions:

$$d_t \bar{p}_h = 0 \text{ if } (\bar{F}_e, \bar{F}_c = 0), \quad (28)$$

$$d_t \bar{H} = 0 \text{ if } (\bar{F}_e, \eta_0, \eta_1, \eta_2, \eta_3 = 0, \\ \partial_t \bar{T}, \partial_t \mathcal{B}, \partial_t \bar{m}_h, \partial_t \bar{\kappa}, \partial_t \alpha, \partial_t \bar{x}_h = 0). \quad (29)$$

The numerical scheme will be constructed such that the discrete counterparts of  $\bar{H}$  and  $\bar{p}_h$  are conserved under the same conditions.

### 3. NUMERICAL FORMULATION

#### 3.1. Difference and Averaging Operators

The numerical model will evaluate variables and parameters at discrete-time instants  $t_n = n\Delta_t$ . The usual form  $u^n$  is employed to denote the approximation to  $u$  at time  $t = n\Delta_t$ . The following shift operators are defined:

$$\epsilon_{t+} u^n = u^{n+\frac{1}{2}}, \quad \epsilon_{t-} u^n = u^{n-\frac{1}{2}}. \quad (30)$$

Elemental temporal difference and averaging operators can then be constructed as

$$\delta_t = \frac{\epsilon_{t+} - \epsilon_{t-}}{\Delta_t}, \quad \mu_t = \frac{\epsilon_{t+} + \epsilon_{t-}}{2}, \quad \delta_t^2 = \frac{\epsilon_{t+}^2 - \epsilon_{t-}^2}{2\Delta_t}, \quad (31)$$

$$\delta_{t+} = \frac{\epsilon_{t+}^2 - 1}{\Delta_t}, \quad \delta_{t-} = \frac{1 - \epsilon_{t-}^2}{\Delta_t}, \quad \mu_t^2 = \frac{\epsilon_{t+}^2 + \epsilon_{t-}^2}{2}. \quad (32)$$

where we can identify several equivalences (e.g.  $\delta_t = \delta_t \mu_t$ ). Finite-difference approximations are achieved by either combining or directly applying these elemental operators, e.g.

$$\delta_t^2 u^n = \frac{u^{n+1} - 2u^n + u^{n-1}}{\Delta_t^2} = \partial_t^2 u(n\Delta_t) + O(\Delta_t^2), \quad (33)$$

$$\mu_t^2 u^n = \frac{u^{n+1} + 2u^n + u^{n-1}}{4} = u(n\Delta_t) + O(\Delta_t^2), \quad (34)$$

$$\delta_t u^n = \frac{u^{n+1} - u^{n-1}}{2\Delta_t} = \partial_t u(n\Delta_t) + O(\Delta_t^2). \quad (35)$$

The following product identities can be derived for arbitrary grid functions  $u^n, q^n$ :

$$\delta_t \{(\delta_t u^n)^2\} = 2\delta_t u^n \delta_t^2 u^n, \quad \delta_t \{(\mu_t u^n)^2\} = 2\delta_t u^n \mu_t^2 u^n, \quad (36)$$

$$\delta_t \{\mu_t q^n \delta_t u^n\} \delta_t u^n = \frac{1}{2} \delta_t \{\mu_t q^n (\delta_t u^n)^2\} + \delta_t q^n \delta_{t+} u^n \delta_{t-} u^n, \quad (37)$$

which is useful for the purposes of numerical energy analysis.

#### 3.2. Discretisation

Let  $\mathbf{u}^n$  be a column vector holding the modal displacements  $\tilde{u}_i^n$ ,  $i = 1, 2, \dots, M$ . The size of this vector (i.e.  $M$ ) will not be varied on-line. Taking into account the need to avoid both numerical dispersion and mode aliasing, the mode dynamics in (21) with time-varying parameters can be discretised in vector form as follows:

$$\delta_t^2 \mathbf{u}^n + \hat{\mathbf{R}}^n \delta_t \mathbf{u}^n + \mu_t^2 \hat{\mathbf{K}}^n \mu_t^2 \mathbf{u}^n = \bar{F}_c \mu_t \mathbf{h}^n, \quad (38)$$

where the non-zero elements of the adjusted diagonal matrices  $\hat{\mathbf{R}}^n$  and  $\hat{\mathbf{K}}^n$  are

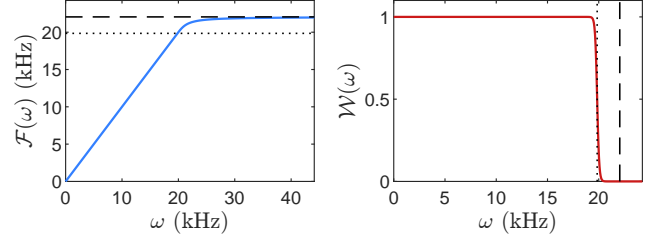


Figure 3: The mode frequency soft-clipping function  $\mathcal{F}(\omega)$  (left) and the suppression weight function  $\mathcal{W}(\omega)$  (right) for  $\Delta_t = 1/44100$ . The dashed line indicates the Nyquist frequency ( $\pi/\Delta_t$ ), and the dotted line represents the cut-off frequency ( $\omega_a$ ).

$$\hat{R}_{i,i}^n = \frac{2b_i^n}{\Delta_t}, \quad \hat{K}_{i,i}^n = \frac{4}{\Delta_t^2} a_i^n. \quad (39)$$

The real-valued coefficients in (39) are:

$$a_i^n = \frac{1 - (\Upsilon_{+,i}^n + \Upsilon_{-,i}^n) + \Upsilon_{+,i}^n \Upsilon_{-,i}^n}{1 + (\Upsilon_{+,i}^n + \Upsilon_{-,i}^n) + \Upsilon_{+,i}^n \Upsilon_{-,i}^n}, \quad (40)$$

$$b_i^n = \frac{2 - 2\Upsilon_{+,i}^n \Upsilon_{-,i}^n}{1 + (\Upsilon_{+,i}^n + \Upsilon_{-,i}^n) + \Upsilon_{+,i}^n \Upsilon_{-,i}^n}, \quad (41)$$

featuring the complex-conjugate pair

$$\Upsilon_{\pm,i}^n = \exp \{ \pm j \mathcal{F}(\omega_i^n) \Delta_t - \frac{1}{2} R_{i,i}^n \Delta_t \}, \quad (42)$$

where  $j = \sqrt{-1}$  and

$$\mathcal{F}(\omega) = \begin{cases} \omega & : \omega^2 < \omega_a^2 \\ \zeta \arctan[\zeta^{-1}(\omega - \omega_a)] + \omega_a & : \text{otherwise} \end{cases} \quad (43)$$

is a function that ‘soft-clips’ the mode frequencies (see the plot on the left-hand side of Figure 3), as such preventing aliased mode frequencies. Here  $\omega_a$  is an appropriate ‘cut-off frequency’ chosen below the Nyquist frequency ( $\omega_a = 0.9\pi/\Delta_t$  is used throughout the paper), and  $\zeta = 2/\Delta_t - 2\omega_a/\pi$ . Since the ‘out-of-range’ modes will have incorrect resonance frequencies, they need to be suppressed in the calculation of both  $\bar{u}_s$  and  $\bar{F}_s$ . This can be achieved by calculating the elements of the vectors  $\mathbf{h}^n$  and  $\mathbf{w}^n$  as  $h_i^n = \mathcal{W}(\omega_i^n) \cdot v_i(\bar{x}_h^n)$  and  $w_i^n = \mathcal{W}(\omega_i^n) \cdot w_i(n\Delta_t)$ , respectively, where  $\mathcal{W}(\omega)$  is a smooth weight function

$$\mathcal{W}(\omega) = \frac{1}{1 + [\text{Re}(\omega)/\omega_a]^{200}}, \quad (44)$$

which strongly suppresses frequencies larger than  $\omega_a$  (see the plot on the right-hand side of Figure 3). Using (24), it can be shown that  $|\Upsilon_{\pm,i}^n| \leq 1$  for both under- and over-damped modes. It follows from (40,41) that  $a_i^n \geq 0$  and  $b_i^n \geq 0$ , meaning that the diagonal elements of  $\hat{\mathbf{R}}^n$  and  $\hat{\mathbf{K}}^n$  are guaranteed non-negative. For constancy in the mode frequencies  $\omega_i^n$ , the above discretisation results into a scheme free of numerical dispersion and attenuation, similarly to the modal-form schemes proposed in previous studies [22, 2]. Expanding (38), one may derive the update form

$$\mathbf{u}^{n+1} = \mathbf{u}^{n-1} + \mathbf{C}^n \mu_t \mathbf{h}^n \bar{F}_c^n - 2\mathbf{z}^n, \quad (45)$$

with

$$\mathbf{z}^n = \frac{1}{2} [\mathbf{B}^n \mathbf{u}^{n-1} - \mathbf{A}^n \mathbf{u}^n], \quad (46)$$

where the elements of the diagonal matrices  $\mathbf{A}^n$ ,  $\mathbf{B}^n$ , and  $\mathbf{C}^n$  are:

$$A_{i,i}^n = \frac{2 - 2\mu_t^2 a_i^n}{1 + \mu_t^2 a_i^n + \mu_t^2 b_i^n}, \quad (47)$$

$$B_{i,i}^n = \frac{2 + 2\mu_t^2 a_i^n}{1 + \mu_t^2 a_i^n + \mu_t^2 b_i^n}, \quad (48)$$

$$C_{i,i}^n = \frac{\Delta_t^2}{1 + \mu_t^2 a_i^n + \mu_t^2 b_i^n}. \quad (49)$$

The hammer dynamics in (10) are discretised with:

$$\delta_t \{ \mu_t \bar{m}_h^n \delta_t \bar{u}_h^n \} = \bar{F}_e^n - \bar{F}_c^n. \quad (50)$$

Setting  $\xi_h^n = \Delta_t^2 / \mu_t \bar{m}_h^{n+\frac{1}{2}}$  and  $\gamma^n = \mu_t \bar{m}_h^{n-\frac{1}{2}} / \mu_t \bar{m}_h^{n+\frac{1}{2}}$ , this can be written as

$$\bar{u}_h^{n+1} = \bar{u}_h^{n-1} - \xi_h^n \bar{F}_c^n - 2z_h^n, \quad (51)$$

where

$$z_h^n = \frac{1}{2} (1 + \gamma^n) (\bar{u}_h^{n-1} - \bar{u}_h^n) - \frac{1}{2} \xi_h^n \bar{F}_e^n. \quad (52)$$

By pre-multiplying (45) with  $(\mathbf{h}^n)^T$  and subtracting (50), the following scalar equation is obtained:

$$\underbrace{\bar{y}^{n+1} - \bar{y}^{n-1}}_{s^n} = \underbrace{\left[ (\mathbf{h}^n)^T \mathbf{C}^n \mu_t \cdot \mathbf{h}^n + \xi_h^n \right]}_{\xi^n} \bar{F}_c^n - 2 \underbrace{\left[ (\mathbf{h}^n)^T \mathbf{z}^n - z_h^n \right]}_{z^n}. \quad (53)$$

The contact force  $\bar{F}_c^n$  as written in quadratised form in (16) is discretised with:

$$\bar{F}_c^n = -(\mu_t \psi^n) \cdot g_{\bar{y}}^n, \quad \frac{\delta_t \psi^n - g_{\bar{\kappa}}^n \delta_t \bar{\kappa}^n - g_{\alpha}^n \delta_t \alpha^n}{\delta_t \bar{y}^n} = g_{\bar{y}}^n, \quad (54)$$

where we can substitute  $2\Delta_t \delta_t \bar{y}^n = s^n$ . From the second equation, a separate update of the auxiliary variable is found as

$$\psi^{n+\frac{1}{2}} = \psi^{n-\frac{1}{2}} + \frac{1}{2} g_{\bar{y}}^n s^n + \frac{1}{2} \underbrace{\left[ g_{\bar{\kappa}}^n (\bar{\kappa}^{n+1} - \bar{\kappa}^{n-1}) + g_{\alpha}^n (\alpha^{n+1} - \alpha^{n-1}) \right]}_{\chi^n}. \quad (55)$$

Substituting the first equation in (54) into (53) we then can, making use of (55), obtain the explicit solution

$$s^n = - \frac{2z^n + \xi^n \left( \psi^{n-\frac{1}{2}} + \frac{1}{2} \chi^n \right) g_{\bar{y}}^n}{1 + \frac{1}{4} \xi^n (g_{\bar{y}}^n)^2}, \quad (56)$$

where it is seen that the denominator in (56) is guaranteed positive, hence solution existence is ensured. Under the assumption that the auxiliary variable remains non-negative during simulation, the gradient variables  $g_{\bar{\kappa}}^n$  and  $g_{\alpha}^n$  can be calculated directly as per equations (17,18). The remaining gradient variable  $g_{\bar{y}}^n$  then has to be constrained such that  $\psi^{n+\frac{1}{2}} \geq 0$ , which in the time-variant case translates to satisfying the quadratic inequality

$$\frac{1}{4} \psi^{n-\frac{1}{2}} \xi^n (g_{\bar{y}}^n)^2 + z^n g_{\bar{y}}^n - \left( \psi^{n-\frac{1}{2}} + \chi^n \right) \leq 0. \quad (57)$$

This leads to the evaluation of  $g_{\bar{y}}^n$  in branched form as given in the Appendix. Once  $s^n$  has been calculated, the auxiliary variable is updated with (55). The  $[\cdot]_+$  operator is subsequently applied to ensure that the value of  $\psi^{n+\frac{1}{2}}$  does not become ever so slightly

negative due to finite-precision errors. Next, the contact force  $\bar{F}_c^n$  is calculated with (54), after which the state variables  $\mathbf{u}$  and  $u_h$  can be updated with (45) and (50), respectively. Finally, the output signal is calculated with  $\bar{F}_s^n = (\mathbf{w}^n)^T \mathbf{u}^n$ . Note that the matrices  $\hat{\mathbf{K}}^n$  and  $\hat{\mathbf{R}}^n$  are not calculated within the algorithm; this is needed only in instances where one wants to track the evolution of the system energy. The update of the modal displacements requires only the elements expressed in (47-49).

### 3.3. Non-Adhesive Contact Force

For the explicit scheme presented above, guaranteed non-adhesion can be shown starting from the inequality  $\psi^{n+\frac{1}{2}} \geq 0$  for all  $n$ , from which it follows that  $\mu_t \psi^n \geq 0$ . From (61) we have that  $\dot{g}_{\bar{y}}^n \geq 0$  by definition. Further, given that the numerator of (62) is non-negative, it follows that  $\dot{g}_{\bar{y}}^n \geq 0$ . Seen together with (60) this means that  $g_{\bar{y}}^n \geq 0$ , and therefore that  $\bar{F}_c^n = -\mu_t \psi^n g_{\bar{y}}^n \leq 0$ .

### 3.4. Energy Balance and Conserved Quantities

From (50) it is immediately clear that the numerical hammer momentum  $\bar{p}_h^{n+\frac{1}{2}} = \mu_t \bar{m}_h^{n+\frac{1}{2}} \delta_t \bar{u}_h^{n+\frac{1}{2}}$  is conserved when no forces act upon the hammer. A discrete energy balance can be derived by pre-multiplying (38) with  $(\delta_t \mathbf{u}^n)^T$ , (50) with  $\delta_t u_h^n$  and adding the resulting equations:

$$\begin{aligned} \delta_t \bar{H}^n &= \frac{1}{4} (\mu_t \mathbf{u}^{n+\frac{1}{2}})^T \delta_t \hat{\mathbf{K}}^n \mu_t \mathbf{u}^{n+\frac{1}{2}} + \frac{1}{4} (\mu_t \mathbf{u}^{n-\frac{1}{2}})^T \delta_t \hat{\mathbf{K}}^n \mu_t \mathbf{u}^{n-\frac{1}{2}} \\ &\quad - (\delta_t \mathbf{u}^n)^T \hat{\mathbf{R}}^n \delta_t \mathbf{u}^n + \delta_t u_h^n \bar{F}_e^n - \delta_t \bar{m}_h^n \delta_t u_h^n - \delta_t \bar{u}_h^n \delta_t u_h^n \\ &\quad - \bar{F}_c^n (\delta_t \mathbf{h}^n)^T \mu_t \mathbf{u}^n + \mu_t \psi^n (g_{\bar{\kappa}}^n \delta_t \bar{\kappa}^n + g_{\alpha}^n \delta_t \alpha^n), \end{aligned} \quad (58)$$

$$\begin{aligned} \bar{H}^{n+\frac{1}{2}} &= \frac{1}{2} (\delta_t \mathbf{u}^{n+\frac{1}{2}})^T \delta_t \mathbf{u}^{n+\frac{1}{2}} + \frac{1}{2} (\mu_t \mathbf{u}^{n+\frac{1}{2}})^T \hat{\mathbf{K}}^{n+\frac{1}{2}} \mu_t \mathbf{u}^{n+\frac{1}{2}} \\ &\quad + \frac{1}{2} \mu_t \bar{m}_h^{n+\frac{1}{2}} (\delta_t \bar{u}_h^{n+\frac{1}{2}})^2 + \frac{1}{2} (\psi^{n+\frac{1}{2}})^2 \geq 0. \end{aligned} \quad (59)$$

Here we made use of the product identities in (36-37). It follows directly that the numerical energy  $\bar{H}^{n+\frac{1}{2}}$  is conserved for constant parameters and no damping or external force. Further, the terms on both sides of (58) are consistent approximations to the corresponding terms in (26), so we can expect the simulation to exhibit energy behaviour under parameter time-variance that approximates that of the underlying continuous-domain model (see Figure 6 for a numerical verification).

### 3.5. Blockwise Parameter Updates & Linear Interpolation

Under the assumption that the control parameters vary over time relatively slowly, they can be updated every  $N_b$  samples, such that the control rate is  $N_b$  times lower than the audio sampling rate, in which case the parameter signals are assumed to be bandlimited in the sense of containing no frequency components above  $f = 1/(2N_b \Delta_t)$ . Given that one round of updating of the model parameters is computationally more expensive than one time step of updating the state variables, such a blockwise parameter update form yields significant computational savings. To alleviate audible artefacts, the following parameters and coefficients are linearly interpolated over each block, at very low cost:  $\bar{m}_h$ ,  $\bar{\kappa}$ ,  $\alpha$ ,  $h_i$ ,  $a_i$ ,  $b_i$ . The coefficients  $\xi_h$  and  $\gamma_h$  as well as the diagonals of  $\mathbf{A}$ ,  $\mathbf{B}$ , and  $\mathbf{C}$  are updated at each time step using the aforementioned linearly-interpolated values.

## 4. NUMERICAL EXPERIMENTS

### 4.1. Contact Force Signals with Static Parameters

Before exploring parameter time-variance, we first verify the correctness of the algorithm and its implementation for the case of constant parameters. Figure 4 shows the contact force signal for three hammer striking velocities, using a standard audio rate (i.e.  $\Delta_t = 1/44100$  s). The resulting waveforms are similar to those obtained in previous studies (e.g. [20]).

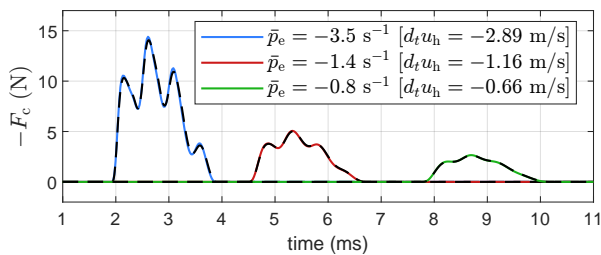


Figure 4: Contact force signals for a C4 string with static parameters. For each hammer velocity, the black dashed line indicates the exact solution as approximated with 24 times oversampling.

### 4.2. String Tuning

Of special interest is the behaviour of the algorithm under time-varying tension, because this involves string modes moving out of and into the normal frequency range of interest. Figure 5 shows the amplitude normalised spectrograms of four simulation output signals. In each simulation, the string was excited with a hard hammer ( $\mathcal{K} = 100000 \text{ s}^{-2}$ ,  $\alpha = 1.2$ ) at  $t = 0.2$  s, and the parameter  $\check{f}_1$  was subsequently increased upwards in a linear fashion by a factor of 1.5, and then linearly decreased back to its original value. The time step is  $\Delta_t = 1/(OF \cdot 44100)$  s, where OF is the oversampling factor. The top left plot, obtained with two times oversampling, can be considered as the nominally correct result. For wider comparison we also include the result obtained with the dynamic grid model [3], for which  $N_b = 1$ . Visible in the top right plot ( $N_b = 1$ ) is the suppression of the out-of-range modes according to the weight function  $\mathcal{W}(\omega)$ . High-frequency artefacts appear with  $N_b = 128$  (bottom left plot), but these are generally more than 60 dB below the level of the partial tones, and as such barely or not audible. A noticeable difference with the FD dynamic grid result is that the mode frequencies evolve in a more regular fashion, and as such the proposed methodology does not rely on frequency-dependent damping and/or oversampling to mask audible artefacts. Secondly, with the modal-form algorithm the modes that drift out of range when the tension increases are ‘pulled back’ into range once the tension is reduced.

### 4.3. Energy and Output Amplitude

A similar experiment is conducted here, this time with no string damping, to investigate the behaviour of the output amplitude and the numerical energy under time-varying tension. Figure 6(b) shows the output signal as calculated with  $w_i$  and  $\dot{w}_i$ , respectively, confirming that the use of adjusted output weights helps reducing output amplitude swings. Figure 6(c) compares the corresponding numerical energy evolution as calculated with oversampling factors

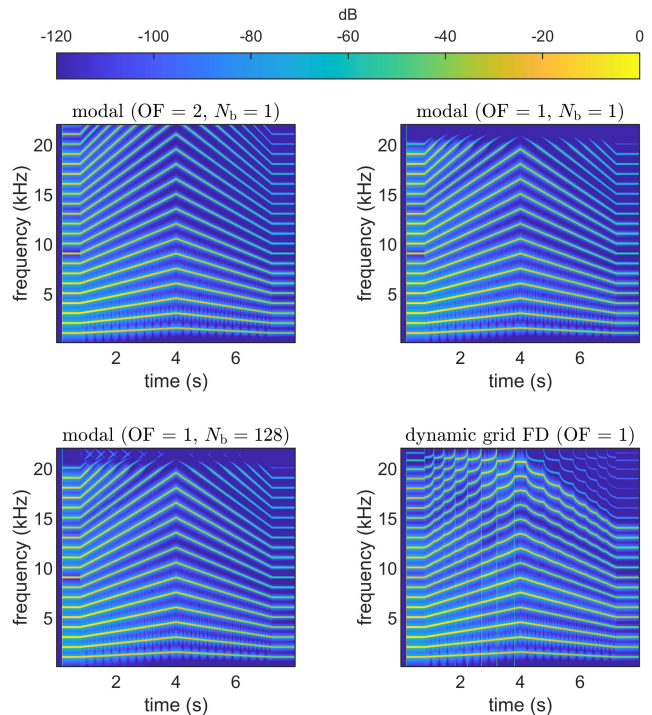


Figure 5: Spectral evolution of the string force signal under time-varying tension. The model parameters are  $\check{f}_1 = 1000$  Hz,  $\mathcal{B} = 2.55 \times 10^{-6}$ ,  $\eta_0 = 0.5 \text{ s}^{-1}$ ,  $\eta_1 = 0 \text{ s}^{-1}$ ,  $\eta_2 = 0.0001 \text{ s}^{-1}$ ,  $\eta_3 = 0 \text{ s}^{-1}$ ,  $\bar{m}_h = 0.3$ ,  $\bar{x}_h = 1/23$ .

$OF = 1$  and  $OF = 24$ , in both cases using  $M = 60$ . The closeness of these two curves demonstrates that the numerical balance remains approximately correct in the presence of mode-frequency soft-clipping (which occurs only for  $OF = 1$  here) and other approximation errors.

### 4.4. Time-Varying Contact Parameters

Among less conventional forms of parameter time-variance, the terrain of on-the-fly adjustment of the contact parameters seems particularly uncharted. To investigate how the algorithm handles such time-variance, single hammer-string collisions were simulated in which the effective stiffness parameter  $\mathcal{K}$  was set to either rapidly increase (see the left-hand side plots of Figure 7) or rapidly decrease (see the right-hand side plots of Figure 7) during contact. As can be seen in the bottom plots, time-variance in  $\mathcal{K}$  leads to hysteresis in the force-vs-compression curve. For increasing  $\mathcal{K}$ , the hysteresis is ‘inverted’ (i.e. in the opposite direction to what is normally observed with hysteresis in piano hammers due to loss mechanisms). The main take-away from these results is that fast time-variance in  $\mathcal{K}$  – and indeed in  $\alpha$ , which was also tested but not shown here – can be simulated without artefacts.

### 4.5. Computational Efficiency

To assess the viability of real-time implementation, the real-time factor (RTF), which is defined here as a measure of how much real time passes with the computation of one second of audio output, was recorded for a range of  $N_b$  and  $M$  values. The piano C2 pa-

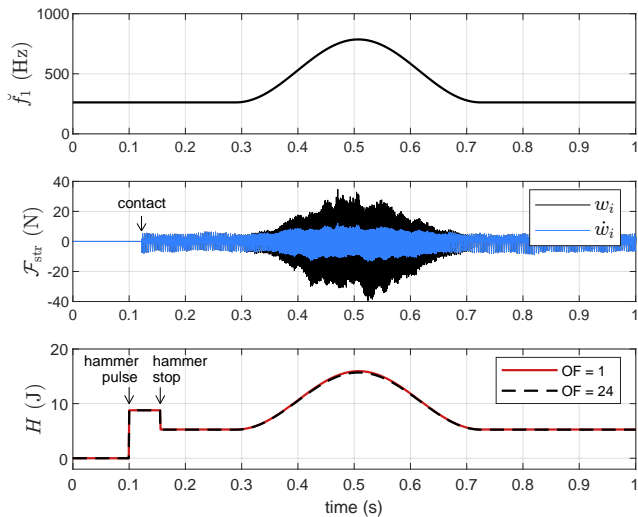


Figure 6: Simulation with time-varying tension and no damping. Top: fundamental frequency profile. Middle: output waveforms for  $OF = 1$ . Bottom: system energy. The parameters are those for a piano C4 string, with  $\Delta_t = 1/(OF \cdot 44100)$  s and  $N_b = 32$ .

rameters listed in Table 1 were used in the simulations, applying regular hammering with randomised hammer velocities across 0.5 s simulation time. For each set ( $N_b$ ,  $M$ ), the RTF was calculated as an average over 50 simulations. The computations were performed in Matlab on an Intel i7-6700 CPU. As can be seen from the results presented in Figure 8, the RTF remains below 0.75 for block sizes of 32 and above with up to 1000 string modes. For reference, the number of modes needed to cover the audio range for an A0, which is the lowest key on standard pianos, is about 300. Because of the uncoupled structure of the modal update form, significant efficiency gains compared to Matlab implementations can be made utilising parallel processing methods in optimised C++ implementations. Examples include the use of Advanced Vector Extensions (see, e.g. [2]).

## 5. CONCLUSION

A numerical scheme for simulating hammer-string interaction with time-varying parameters has been formulated in modal form. As part of adapting the energy quadratisation approach to modelling collisions under parameter time variance, two new gradient variables were introduced. The physical correctness of the algorithm is underpinned by the numerical contact force being provably non-adhesive and by the existence of a numerical energy balance, the form of which directly mirrors that of the continuous-domain model.

With respect to handling time-varying string tension, modes with frequencies that exceed the available frequency bandwidth for a given time step remain active within the numerical model, with their frequencies adjusted to fall into a narrow frequency band just below the Nyquist frequency. These out-of-range modes continue to contribute to the overall system energy (hence a numerical energy balance exists) but are suppressed in the calculation of the output signal and of the string displacement at the hammer position and as such do not interfere with the sound synthesis process while they are out of range. In addition, a pragmatic form of re-scaling of the output force signal under time-variance in the string tension

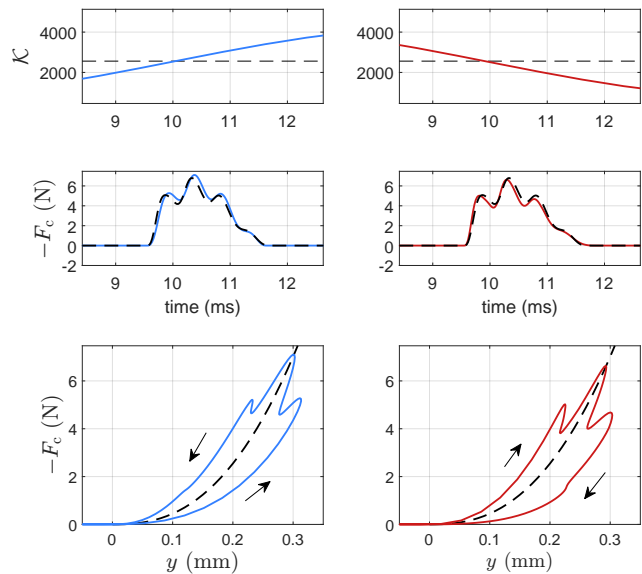


Figure 7: Simulation with time-variation in the contact stiffness parameter ( $\mathcal{K}$ ). Left: increasing stiffness. Right: decreasing stiffness. In each subplot, the dashed line indicates the simulation with constant  $\mathcal{K}$ . The parameters are those for a piano C4 string, with  $\Delta_t = 1/44100$  s and  $N_b = 32$ .

was introduced to avoid large amplitude fluctuations, meaning a much reduced need to make adjustments to the output gain.

The off-line numerical experiments conducted within this work indicate that the algorithm’s computational load is sufficiently small for real-time implementation and that no audible artefacts arise under parameter time-variance. More exhaustive testing on the latter point is still required though, and this is perhaps best done through on-line control. A real-time controlled implementation will also provide better opportunities to explore the possibilities that the proposed model can offer as the sound engine of a (live-performable) virtual-acoustic musical instrument.

## 6. ACKNOWLEDGMENTS

This work was supported by the European Union’s Horizon 2020 research and innovation programme under the Marie Skłodowska-Curie grant agreement No 812719.

## 7. REFERENCES

- [1] S. Mehes, M. van Walstijn, and P. Stapleton, “Virtual-Acoustic Instrument Design: Exploring the Parameter Space of a String-Plate Model,” in *New Interfaces for Musical Expression*, Copenhagen, 2017, pp. 399–403.
- [2] M. van Walstijn and S. Mehes, “An explorative string-bridge-plate model with tunable parameters,” in *20th Int. Conf. on Digital Audio Effects (DAFx-17)*, 2017, pp. 291–298.
- [3] S. Willemsen, S. Bilbao, M. Ducceschi, and S. Serafin, “The dynamic grid: time-varying parameters for musical instrument simulations based on finite-difference time-domain schemes,” *J. Aud. Eng. Soc.*, vol. 70, no. 9, pp. 650–660, september 2022.

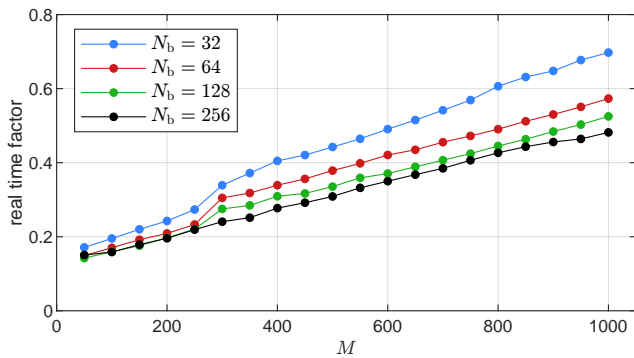


Figure 8: Matlab real-time factor for specific combinations of number of modes ( $M$ ) and block size ( $N_b$ ).

[4] J. Pakarinen, T. Puputti, and V. Välimäki, “Virtual Slide Guitar,” *Computer Music Journal*, vol. 32, no. 3, pp. 42–54, 09 2008.

[5] C. Cadoz, A. Luciani, and J. Florens, “Cordis-anima: A modeling and simulation system for sound and image synthesis: The general formalism,” *Computer Music Journal*, vol. 17, no. 1, pp. 19–29, 1993.

[6] J. Morrison and J. Adrien, “Mosaic: A framework for modal synthesis,” *Computer Music Journal*, vol. 17, no. 1, pp. 45–56, 1993.

[7] S. Bilbao and A. Torin, “Numerical simulation of string/barrier collisions: The fretboard,” in *Proc. of the 17th Int. Conf. on Digital Audio Effects (DAFx-14)*, Erlangen, Germany, September 1-5, 2014, 2014, pp. 137–144.

[8] C. Desvages and S. Bilbao, “Two-polarisation physical model of bowed strings with nonlinear contact and friction forces, and application to gesture-based sound synthesis,” *Applied Sciences*, vol. 6, no. 5, 2016.

[9] S. Bilbao, J. Perry, P. Graham A. Gray, K. Kavoussanakis, G. Delap, T. Mudd, G. Sassoon T. Wishart, and S. Young, “Large-Scale Physical Modeling Synthesis, Parallel Computing, and Musical Experimentation: The NESS Project in Practice,” *Computer Music Journal*, vol. 43, no. 2-3, pp. 31–47, 2019.

[10] A. Bhanuprakash, M. van Walstijn, and P. Stapleton, “A finite difference model for articulated slide-string simulation,” in *Proc. Int. Conf. Digital Audio Effects (DAFx-20)*, Sept. 2020, pp. 195–202, University of Music and Performing Arts Vienna.

[11] N. Lopes, T. Hélie, and A. Falaize, “Explicit second-order accurate method for the passive guaranteed simulation of port-Hamiltonian systems,” in *5th IFAC Workshop on Lagrangian and Hamiltonian Methods for Nonlinear Control LHMNC 2015*, Lyon, France, July 2015, IFAC, vol. 48 of *IFAC-PapersOnLine*, pp. 223–228.

[12] J. Zhao, Q. Wang, and Z. Yang, “Numerical approximations for a phase field dendritic crystal growth model based on the invariant energy quadratization approach,” *Int. J. Num. Meth. Eng.*, vol. 110, no. 3, pp. 279–300, 2017.

[13] J. Shen, J. Xu, and J. Yang, “The scalar auxiliary variable (SAV) approach for gradient flows,” *J. Computational Physics*, vol. 353, pp. 407–416, 2018.

[14] M. Ducceschi and S. Bilbao, “Simulation of the geometrically exact nonlinear string via energy quadratisation,” *J. Sound and Vibr.*, vol. 534, pp. 117021, 2022.

[15] S. Bilbao, M. Ducceschi, and F. Zama, “Explicit exactly energy-conserving methods for hamiltonian systems,” *J. Computational Physics*, vol. 472, pp. 111697, 2023.

[16] M. Ducceschi and S. Bilbao, “Non-iterative solvers for nonlinear problems: the case of collisions,” in *Proc. of the 22nd Conf. of Digital Audio Effects (DAFx-19)*, Birmingham, UK, September 2019, pp. 17–24.

[17] M. Ducceschi, S. Bilbao, S. Willemsen, and S. Serafin, “Linearly-implicit schemes for collisions in musical acoustics based on energy quadratisation,” *J. Acoust. Soc. Am.*, vol. 149, no. 5, pp. 3502–3516, 2021.

[18] A. Chaigne and A. Askenfelt, “Numerical simulations of piano strings. I. A physical model for a struck string using finite difference methods,” *J. Acoust. Soc. Am.*, vol. 95, pp. 1112–1118, 1994.

[19] N. H. Fletcher and T. D. Rossing, *The Physics of Musical Instruments*, Springer-Verlag, New York, 1991, Second Edition: 1998.

[20] A. Chaigne and A. Askenfelt, “Numerical simulations of piano strings. II. Comparisons with measurements and systematic exploration of some hammer-string parameters,” *J. Acoust. Soc. Am.*, vol. 95, no. 3, pp. 1631–1640, 1994.

[21] J. Woodhouse, “Plucked guitar transients: Comparison of measurements and synthesis,” *Acta Acustica united with Acustica*, vol. 90, no. 5, pp. 945–965, 2004.

[22] M. van Walstijn, J. Bridges, and S. Mehes, “A Real-Time Synthesis Oriented Tanpura Model,” in *Proc. Int. Conf. Digital Audio Effects (DAFx-16)*, 2016, pp. 175–182.

## 8. APPENDIX: BRANCHED EVALUATION OF $g_{\bar{y}}^n$

For the update equations (55,56), the gradient variable  $g_{\bar{y}}^n$  is calculated as

$$g_{\bar{y}}^n = \begin{cases} \min(\dot{g}_{\bar{y}}^n, \dot{g}_{\bar{y}+}^n) & : \bar{y}^n > 0 \\ \dot{g}_{\bar{y}+}^n & : \bar{y}^n < 0 \quad \& \quad \bar{y}^{n-1} > 0 \\ 0 & : \text{otherwise} \end{cases}, \quad (60)$$

where  $\dot{g}_{\bar{y}}^n$  denotes the nominal value according to (17):

$$\dot{g}_{\bar{y}}^n = g_{\bar{y}}(\bar{y}^n) = \sqrt{\frac{1}{2}\bar{\kappa}^n(\alpha^n + 1)[\bar{y}^n]_+^{\alpha^n - 1}}. \quad (61)$$

The term  $\dot{g}_{\bar{y}+}^n$  is the positive root of the quadratic term on the left-hand side of (57) that needs to remain non-positive to ensure that  $\psi^{n+\frac{1}{2}} \geq 0$ :

$$\dot{g}_{\bar{y}+}^n = 2 \frac{-z^n + \sqrt{(z^n)^2 + \xi^n \psi^{n-\frac{1}{2}} [\psi^{n-\frac{1}{2}} + \chi^n]_+}}{\sqrt{\varepsilon \xi^n (z^n)^2 + (\xi^n \psi^{n-\frac{1}{2}})^2}}. \quad (62)$$

The inclusion of the term  $\varepsilon \xi^n (z^n)^2$  in the denominator, where  $\varepsilon > 0$  is of the order of the machine epsilon, helps ensure that the correct solution is found for  $\psi^{n-\frac{1}{2}} \rightarrow 0$ . The operator  $[\cdot]_+$  is applied within the square root to ensure a real root and that  $\dot{g}_{\bar{y}}^n \geq 0$ . The middle branch in (60) effectively sets  $\psi^{n+\frac{1}{2}}$  to zero at the end of contact, as such altogether avoiding any spurious non-zero contact force values at time instances where there is no contact.